Combustion and Flame 248 (2023) 112576

Contents lists available at ScienceDirect

Combustion and Flame

journal homepage: www.elsevier.com/locate/combustflame

Direct bond fission and hydrogen migration as the trigger forces in the pyrolysis of *n*-pentyl nitrate at low pressure

Tongpo Yu[a,1], Qiang Xu[a,1], Hong Wang[a], Cheng Xie[a], Jiwen Guan[a], Xiaoguo Zhou[b,*], Zhandong Wang[a,c,*]

[a] National Synchrotron Radiation Laboratory, University of Science and Technology of China, Hefei, Anhui 230029, PR China
[b] Hefei National Laboratory for Physical Sciences at the Microscale, Department of Chemical Physics, University of Science and Technology of China, Hefei 230026, PR China
[c] State Key Laboratory of Fire Science, University of Science and Technology of China, Hefei, Anhui 230026, PR China

ARTICLE INFO

Article history:
Received 7 September 2022
Revised 3 December 2022
Accepted 6 December 2022

Keywords:
n-Pentyl nitrate
Pyrolysis
Photoionization efficiency
Synchrotron radiation
Mass spectrometry

ABSTRACT

Nitrates are a potential class of substances as cetane improvers of diesel fuel and are critical raw materials for some military explosives. Thus, an in-depth investigation of the thermal decomposition mechanism of nitrates is important for further improving their effects. Herein, a combination of experimental and computational studies was performed for the pyrolysis of *n*-pentyl nitrate in the temperature range of 400–900 K. Using synchrotron radiation vacuum ultraviolet photoionization, some intermediates and products, such as ethylene, formaldehyde, propene, ethenol, pentanal, NO_2, and HONO, were identified according to their photoionization efficiency curves. Quantum chemical calculations at the CBS-QB3 level were conducted to elucidate the overall reaction mechanism of *n*-pentyl nitrate pyrolysis. Along the direct bond fission of *n*-pentyl nitrate, primary products, $C_5H_{11}O$• radical and NO_2, and butyl radical and CH_2ONO_2, can further dissociate into many products, in which formaldehyde is the most dominant. In addition, two hydrogen-atom migration channels followed by decomposition are verified for the decomposition of *n*-pentyl nitrate according to the observation of *trans*-HONO, pentanal, and 1-pentene. These evidences highlight that both bond fission and hydrogen migration play comparable roles as potential driving forces in the pyrolysis of *n*-pentyl nitrate at low pressure. This thermal decomposition mechanism of *n*-pentyl nitrate provides some useful clues for developing combustion models of long chain nitrates in future.

1. Introduction

Organic nitrates ($RONO_2$), such as nitroglycerine, pentaerythrite, and tetranitrate, are extensively used as explosives and propellants in engineering, rocket launching, and defense construction [1–3]. Organic nitrates usually have a low boiling point and low cetane number (CN) and can generate chain-initiating radicals during decomposition [4,5]. Thus, they can improve the combustion properties of diesel fuel and are commonly used as fuel additives.

To acquire in-depth knowledge about the thermal decomposition kinetics of nitrate ester, some experimental and theoretical investigations have been conducted. Levy and Adrian [6] measured the absorption spectroscopy of major products from the thermal decomposition of n-propyl nitrate at 181 °C, where the nitrogen-containing products were quantified. Approximately equal amounts of n-propyl nitrite and nitromethane were observed, as well as a small quantity of NO and the traced amount of NO_2. In contrast, the cleavage behavior of isopropyl nitrate was quite different due to the presence of substituents on the α-C atom. Griffiths et al. [7,8] performed pyrolysis experiments on isopropyl nitrate in a closed rector using gas chromatography and mass spectrometry. At temperatures below 230 °C and 40 kPa, they observed isopropyl nitrite (44%) and acetaldehyde (42%) as predominant products, with small amounts of acetone, nitromethane, and methyl nitrite. When the temperature was increased to 1030–1280 °C with a high pressure of 1.4 MPa, small molecule products became dominant, e.g., H_2, N_2, CO, CO_2, CH_4, NO and H_2O. A multistep dissociation mechanism was then proposed in which a key intermediate, isopropoxy radical, initially produced from direct RO–NO_2 bond breaking, can react with NO to form isopropyl nitrite, or produce acetaldehyde by CH_3-loss and acetone by H-loss. Recently, Oxley et al. [9] reinvestigated the thermal decomposition of isopropyl nitrate, isopropyl alcohol, acetone, ethanol, and ethanediol, and certain amounts of

* Corresponding authors.
E-mail addresses: xzhou@ustc.edu.cn (X. Zhou), zhdwang@ustc.edu.cn (Z. Wang).
[1] T. Y. and Q. X. contributed equally to this work.

https://doi.org/10.1016/j.combustflame.2022.112576
0010-2180/

Table 1
The primary decomposition pathways of *n*-pentyl nitrate, with the corresponding energies relative to neutral *n*-pentyl nitrate, calculated at the CBS-QB3 level.

	Pathways	relative energy /kcal·mol^{-1}	description
R1	$CH_3(CH_2)_4O\bullet + NO_2$	43.1	N–O bond fission
R2	$CH_3(CH_2)_3CH_2\bullet + \bullet ONO_2$	88.2	C–O bond fission
R3	$CH_3(CH_2)_2CH_2\bullet + \bullet CH_2ONO_2$	52.9	C–C bond fission
R4	$CH_3CH_2CH_2\bullet + \bullet CH_2CH_2ONO_2$	91.5	C–C bond fission
R5	$CH_3CH_2\bullet + \bullet CH_2(CH_2)_2ONO_2$	89.2	C–C bond fission
R6	$CH_3\bullet + \bullet CH_2(CH_2)_3ONO_2$	90.4	C–C bond fission
R7	$CH_3(CH_2)_3CHO$ + *trans*-HONO	−19.3	pentanal formation
R8	$CH_3(CH_2)_2CH{=}CH_2 + HONO_2$	16.0	1-pentene formation

methanol and acetaldehyde were all observed in the gas chromatograph, as well as 2-methyl-2-acrylonitrile. In addition, Pritchardfad et al. [10] studied the pyrolysis of isooctyl nitrate in the temperature range of 198–244 °C. The major products were formaldehyde, acetaldehyde, propionaldehyde, and aldehydes with five carbon atoms. More recently, Morin and Bedjanian et al. [11–13] performed a systematic investigation on the pyrolysis of ethyl, isopropyl, *n*-propyl and *n*–butyl nitrates using flow reaction tubes. For thermal decomposition of these nitrates, the primary product, NO_2, was directly observed with a high yield of nearly unity. The alkoxy radical as the other product of RO–NO_2 bond fission was also identified and quantified, although they were not directly observed in mass spectrometer. In addition, the rate constant of nitrate thermal decomposition was measured as a function of pressure and temperature.

Apparently, there are some inconsistencies with the pyrolysis product species of nitrate in the previous studies, although the rate-controlling step is generally thought to be the homogeneous cleavage of the RO–NO_2 bond to produce NO_2 and alkoxy radicals (RO•), according to its low activation energy of ∼167 kJ/mol [14]. Notably, RO• radicals play a vital role as essential intermediates in combustion and atmospheric chemistry, and they can be further converted to other products via unimolecular decomposition, isomerization, or reaction with oxygen. These diverse reactions triggered by RO• lead to the varied products observed in the previous experiments. It is worth noting that except for NO_2, no directly experimental observation was reported for the other primary products, such as alkoxy radicals from RO–NO_2 bond fission, $\bullet ONO_2$ from C–O bond rupture, and $\bullet CH_2ONO_2$ from C–C bond breaking. Moreover, no complete potential energy surface was reported for the pyrolysis of *n*-pentyl nitrate. Thus, although the pyrolysis rate constants and reaction products of several alkyl nitrates under low pressure and a certain temperature range were measured [11–13], the thermal decomposition mechanism of *n*-pentyl nitrate is still potentially controversial, as secondary reactions might have considerable influence on the observed product species. Consequently, the limited results of the previous studies are not sufficient to support a credible and consistent pyrolysis mechanism of alkyl nitrate over a relatively large temperature range.

In this work, we chose *n*-pentyl nitrate as a representative to reinvestigate the pyrolysis mechanism of organic nitrates with a moderate carbon chain length. To better observe intermediates, we applied a synchrotron vacuum ultraviolet photoionization mass spectrometer (SVUV-PIMS) to detect products and intermediates of *n*-pentyl nitrate pyrolysis in a temperature-controlled microreactor, in which a relatively low pressure was kept to suppress the most secondary reactions as much as possible. By recording and analyzing the photoionization efficiency (PIE) curve of each species, the main products and a few intermediates were identified with the help of well-identified PIE curves of some molecules. With the aid of quantum chemical calculations, the primary thermal decomposition mechanism of *n*-pentyl nitrate is proposed, considering the C–C, C–O and N–O bond breaking, together with isomerization-decomposition steps, as listed in Table 1.

2. Experimental and computational methods

The pyrolysis experiments of *n*-pentyl nitrate were carried out at the atomic & molecular physics beamline (BL09U), National Synchrotron Radiation Laboratory in Hefei. Vacuum ultraviolet (VUV) photons from an undulator of an 800 MeV electron-storage ring were dispersed with a 6 m-long monochromator with a 370 grooves•mm^{-1} spherical grating. The photon energy ranged from 7.0 to 22.5 eV with an energy-resolving power (E/ΔE) of ∼3000 at 15 eV [15]. The experimental setup consisted of a liquid bubble feed system, a temperature-controlled pyrolysis microreactor, a sampling cone unit, a differential vacuum chamber, and a photoionization chamber with a reflectron time-of-flight mass spectrometer (TOF-MS). *n*-Pentyl nitrate (98%) was purchased from Sigma–Aldrich Inc. and was used without further purification. A gas mixture of 0.4% (volume percentage) *n*-pentyl nitrate in helium (5 atm) was prepared in a stainless steel tube at a flow rate of 20 sccm. To identify dissociative photoionization fragments of *n*-pentyl nitrate, the comparative mass spectra were recorded at room temperature without pyrolysis. A temperature-controlled Chen-type pyrolysis microreactor [16] was applied to perform the thermal decomposition of *n*-pentyl nitrate at temperatures up to 900 K. In this microreactor (30 mm long heated silicon carbide tube), the pressure was roughly a few tens of mbar, and the residence time was estimated to be 10–100 μs [17]. The gas mixture from the reactor was expanded to a high vacuum chamber (10^{-4} Pa), where the neutral species were photoionized by VUV photons. More detailed experimental conditions were listed in Table S1 of the supporting information.

The experimental PIE curves of the major products were directly compared with the previously reported curves in the database [18]. By slightly shifting the adiabatic ionization energy (IE_a) value and combining the contributions of isomers at each *m/z*, the best agreement between the present and previous data was obtained and was used to identify the corresponding species. Moreover, the complete basis set model of the CBS-QB3 method [19] was used to calculate the potential energy surface for the unimolecular decomposition of *n*-pentyl nitrate, in which the density functional theory of B3LYP and the 6–311++*G*(d,p) level basis set were used to optimize molecular structures and to calculate vibrational frequencies of all concerned species. The relative energies were calculated as the potential energy after zero-point energy correction using the calculated vibrational frequencies. Intrinsic reaction coordinate (IRC) calculations [20,21] were conducted to validate that the located transition states indeed connect the assumed reactant and product(s). Using the optimized structures of each species, accurate single-point energies were calculated at the CBS-QB3 level. All these quantum chemical calculations were performed using the Gaussian 16 A.03 program package [22].

Table 2
Relative concentrations of dominant species in the temperature range from 500 K to 900 K. [a].

	C_2H_4 (*m/z* 28)	CH_2O (*m/z* 30)	C_3H_6 (*m/z* 42)	C_2H_4O (*m/z* 44)	NO_2 (*m/z* 46)	HNO_2 (*m/z* 47)
500K	0.16%	0.40%	0.15%	0.18%	1.23%	0.39%
600K	0.36%	1.83%	0.47%	0.86%	4.85%	1.42%
700K	11.68%	24.40%	2.36%	8.13%	16.92%	13.86%
800K	21.71%	35.70%	2.51%	8.29%	10.90%	4.35%
900K	23.83%	45.60%	3.41%	7.74%	1.82%	0.12%
	C_4H_8 (*m/z* 56)	C_4H_9 (*m/z* 57)	C_3H_6O (*m/z* 58)	C_5H_8 (*m/z* 68)	C_5H_{10} (*m/z* 70)	$C_5H_{10}O$ (*m/z* 86)
500K	0.17%	94.96%	1.97%	0.01%	0.36%	0.01%
600K	1.04%	85.79%	2.58%	0.26%	0.46%	0.08%
700K	4.14%	10.91%	5.54%	0.83%	0.66%	0.55%
800K	4.03%	6.12%	4.47%	0.88%	0.53%	0.51%
900K	7.29%	4.84%	3.12%	1.21%	0.58%	0.44%

[a] In this experiment, the parent ion of *n*-pentyl nitrate was not detected, so the relative concentrations of pyrolysis products was calculated using the fragment $C_4H_9^+$ instead of the parent ions.

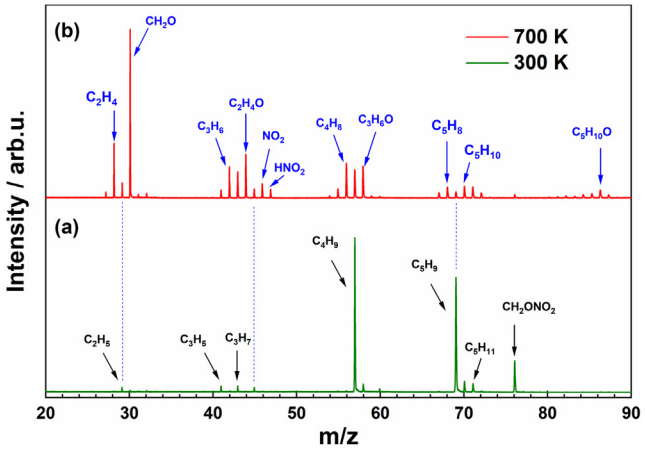

Fig. 1. Photoionization mass spectra of *n*-pentyl nitrate measured at 300 K (a) and in the pyrolysis of *n*-pentyl nitrate at 700 K (b) with the photon energy of 11.5 eV.

3. Results and discussion

3.1. Species pool detected by photoionization mass spectrometer

Figure 1a shows the photoionization mass spectra of *n*-pentyl nitrate at 300 K. We note that the mass peak of *n*-pentyl nitrate at *m/z* 133 is invisible, indicating that the parent ion is unstable and dissociative photoionization naturally occurs. As a result, mass peaks of the fragments $C_2H_5^+$ (*m/z* 29), $C_3H_5^+$ (*m/z* 41), $C_3H_7^+$ (*m/z* 43), $C_4H_9^+$ (*m/z* 57), $C_5H_9^+$ (*m/z* 69), $C_5H_{11}^+$ (*m/z* 71), and $CH_2ONO_2^+$ (*m/z* 76) are clearly observed. Since the dissociative photoionization of *n*-pentyl nitrate is not the main purpose of the current study, we do not discuss the fragmentation mechanism of the *n*-pentyl nitrate ion here.

The photoionization mass spectrum for the pyrolysis of *n*-pentyl nitrate at 700 K is shown in Fig. 1b. The main mass peaks are $C_2H_4^+$ (*m/z* 28), CH_2O^+ (*m/z* 30), $C_3H_6^+$ (*m/z* 42), $C_2H_4O^+$ (*m/z* 44), NO_2^+ (*m/z* 46), HNO_2^+ (*m/z* 47), $C_4H_8^+$ (*m/z* 56), $C_4H_9^+$ (*m/z* 57), $C_3H_6O^+$ (*m/z* 58), $C_5H_8^+$ (*m/z* 68), $C_5H_{10}^+$ (*m/z* 70), and $C_5H_{10}O^+$ (*m/z* 86), most of which are different from those in Fig. 1a. Therefore, these species are undoubtedly mostly generated from the pyrolysis of *n*-pentyl nitrate. Notably, the *m/z* 57 peak appears under both conditions, but according to the relative intensities, such as $C_4H_9^+$:$C_5H_9^+$:$CH_2ONO_2^+$ = 49:39:12 in Fig. 1a and $C_4H_9^+$:$C_5H_9^+$:$CH_2ONO_2^+$ = 76:16:8 in Fig. 1b, we can affirm the formation of $C_4H_9^+$ (*m/z* 57) in pyrolysis, although not all. To further verify this conclusion, we performed a temperature-dependent measurement in the range of 400–900 K, and the corresponding mass spectra are shown in Fig. S1 of the supporting information. Relative concentrations of major species at a few representative temperatures are listed in Table 2, after correction of the amount of *n*-pentyl nitrate in normalization.

Apparently, below 700 K, the pyrolysis products are minor in comparison to those in the dissociative photoionization process, such as $C_4H_9^+$ (*m/z* 57), $C_5H_9^+$ (*m/z* 69), and $CH_2ONO_2^+$ (*m/z* 76). Moreover, nitroalkane as the dominant product observed in previous experiments [6–8] was not detected in this experiment, and hence it might be formed due to secondary reactions at relatively high pressure. When the pyrolysis temperature is increased to 700 K, the pyrolysis products become dominant species in the mass spectra. As shown in Table 2, CH_2O (*m/z* 30) is the most dominant, which generally agrees with previous experiments [7,8]. A certain amount of the other products of *m/z* 28, 42, 44, 46, 47, 56, 57, 58, 68, 70 and 86 were also observed. The experimental concentration of major product CH_2O and C_2H_4 (*m/z* 28), monotonously increases with the pyrolysis temperature (in Table 2). Interestingly, the sum of the C_2H_4 and CH_2O molar ratio remains greater than 50% in the temperature range from 800 to 900 K, while other minor products, such as C_3H_6, C_2H_4O, NO_2, HNO_2, C_4H_8, C_4H_9, C_3H_6O, C_5H_8, C_5H_{10}, and $C_5H_{10}O$, persist with a concentration ratios range of 25% and 36%.

To identify the species observed in the mass spectra, the PIE curves of the major products are presented in Figs. 2 and 3. As the primary products in the pyrolysis of *n*-pentyl nitrate (Table 1), the NO_2 (*m/z* 46), HNO_2 (*m/z* 47), C_4H_9 (*m/z* 57), C_5H_{10} (*m/z* 70) and $C_5H_{10}O$ (*m/z* 86) products were indeed observed. As shown in Fig. 2a, the measured PIE onset for *m/z* 46 is determined to be 9.58 eV, which agrees well with the IE_a of NO_2 in the NIST database [23], 9.586±0.002 eV. Moreover, the present and reported PIE curves of NO_2 measured by Au and Brion [24] are highly consistent in Fig. 2a. Thus, the *m/z* 46 signal is explicitly attributed to the NO_2 molecule. Moreover, our PIE curve of the *m/z* 47 and the PIE curve of *trans*-HONO measured by Taatjes et al. [25] are directly compared with our data of *m/z* 47(HNO_2) in Fig. 2b, and the perfect consistency between the two curves verifies this assignment. As the secondary reactions between NO_2 and those major products, such as formaldehyde, ethylene, aldehyde, propanal, are all endothermic with the reaction heats (ΔH_{298}) of roughly 10–30 kcal/mol, these reactions could not be major contributors to the observed *trans*-HONO in such short residence time. Therefore, the observation of *trans*-HONO provides evidence for the occurrence of the **R7** channel. The PIE onset for *m/z* 47 obtained in our experiment is determined to be 10.94 eV, which provides an upper limit of IE_a (*trans*-HONO). In the PIE curve of *m/z* 57 ($C_4H_9^+$) of Fig. 1c, the onset was observed at ~8.7 eV. This value is ~0.7 eV higher than the reported IE_a (8.02 eV) for 1–butyl radical [26]. In fact, it is not surprising to observe such a higher experimental threshold

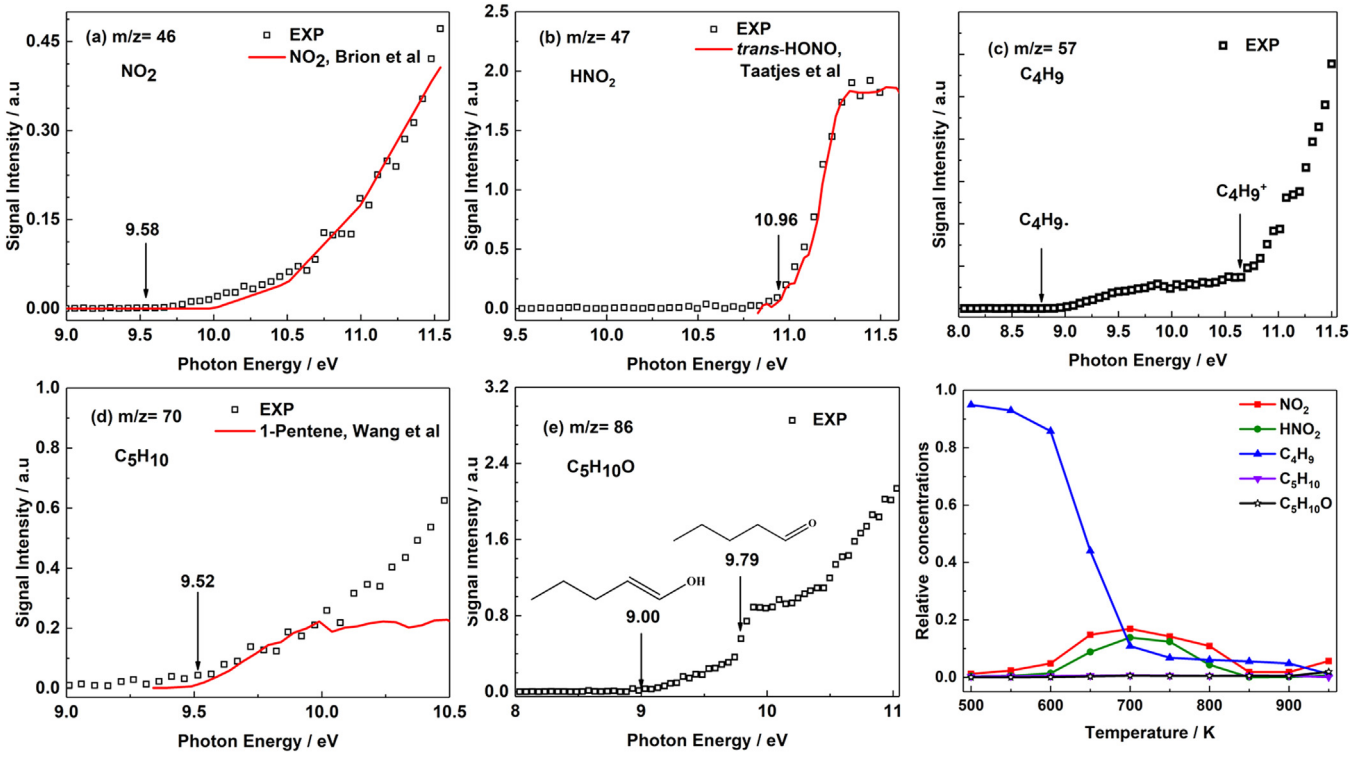

Fig 2. Photoionization efficiency curves for the *m/z* 46, 47, 57, 70, and 86 in the pyrolysis of *n*-pentyl nitrate, as well as the relative concentrations of these products.

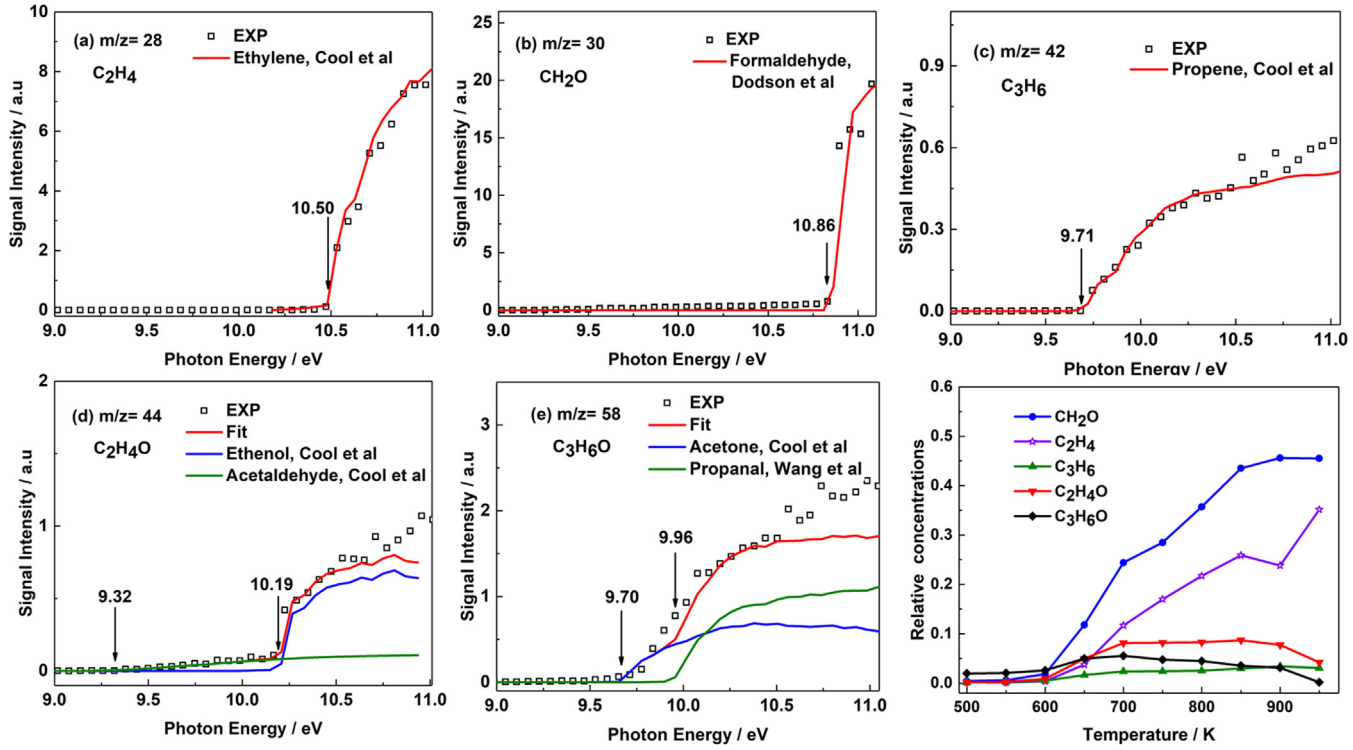

Fig 3. Photoionization efficiency curves for the *m/z* 28, 30, 42, 44, and 58, as well as the relative concentrations of these products in the pyrolysis of *n*-pentyl nitrate.

because of a competition shift in multi-channel decomposition of molecules. We note that the inflection point at ca. 10. 8 eV comes from the photon dissociation of *n*-pentyl nitrate.

For *m/z* 70, the possible candidates in the pyrolysis of *n*-pentyl nitrate are 1-pentene and its isomers, such as cyclopentane, methyl cyclobutane and 1,1-dimethyl cyclopropane. Their IE_a values are reported in the NIST database [26] to be 9.49±0.03 eV for 1-pentene, 10.33±0.15 eV for cyclopentane, 9.64±0.05 eV for methyl cyclobutane, and 8.98±0.05 eV for 1,1-dimethyl cyclopropane. In addition, 3-butenal (C_4H_6O, *m/z* 70, IE_a=9.65 eV) is also probably formed in our reaction system. As shown in Fig. 2d, the PIE onset is located at ~9.5 eV in our experiment, and hence, 1-pentene, as the

R8 product, appears to be the best appropriate contributor. Moreover, the rising edge of the PIE curve can be fitted well with the PIE spectrum of 1-pentene, providing additional evidence for this assignment. Additionally, we note that the *m/z* 70 signal continues to grow consistently above 10.15 eV, which is inconsistent with the plateau in the PIE curve of 1-pentene. Based on the above IE_a values, cyclopentane might contribute to the PIE tail, which could be formed in our reaction system via isomerization from 1-pentene.

In the PIE curve of *m/z* 86 (Fig. 2e), two clear onsets are observed at 9.00 and 9.79 eV, respectively. The higher-energy value readily corresponds to the IE_a value of pentanal (9.74±0.04 eV) [27], which happens to be the other **R7** product in addition to *trans*-HONO, while the product with lower onset can be attributed to one isomer of pentanal, 4-penten-1-ol (IE_a=9.42±0.05 eV in NIST [26]). The lower threshold for 4-penten-1-ol detected in our experiment might be due to the keto-enol isomerization from pentanal. Additionally, Fig. 2f shows the temperature-dependent relative concentrations of these species. With increasing temperature above 700 K, the relative concentrations of almost all primary pyrolysis products decrease.

It is worth noting that the other primary product of **R1**, pentyloxy radical ($C_5H_{11}O$•), was invisible in mass spectra, implying that its decomposition is favorable to proceed. Similarly, the isomerization and dissociation of the aforementioned primary products, $C_5H_{10}O$ (from **R7**) and C_5H_{10} (from **R8**), can also occur. These subsequent reactions produce more products. As shown in Fig. 3a and b, the measured PIE spectra for the two most dominant products, *m/z* 28 and 30, are directly compared with the PIE curves of ethylene [28] and formaldehyde [29]. The excellent agreement between the PIE curves and IE_a values verifies the assignments of ethylene for *m/z* 28 and formaldehyde for *m/z* 30. For the *m/z* 42, the onset at 9.71 eV in Fig. 3c is close to the IE_a of propene (9.73 eV in the NIST database[30]), and moreover, the PIE curve of propene [31] agrees very well with our result, even reproducing the rising edge. These agreements strongly indicate the dominant contribution by propene. In addition, we can attribute the *m/z* 44 signal (Fig. 3d) to ethenol and acetaldehyde because two onsets, 9.32 and 10.19 eV, are consistent with the IE_a values in the database, e.g. 9.33±0.01 eV for ethenol and 10.229±0.007 eV for acetaldehyde. More importantly, the present PIE curve agrees very well with the sum of ethenol and acetaldehyde [31], as shown in Fig. 3d, providing additional evidence for this assignment. A similar scenario is seen in the PIE curve of *m/z* 58, as shown in Fig. 3e. Apparently, the combination of the PIE curves of acetone [28] and propanal [26] can reproduce the currently measured PIE curve of *m/z* 58, suggesting their formation in pyrolysis process. In summary, these dominant products in the mass spectra are confirmed by the analyses of the PIE curves to be ethylene (*m/z* 28), formaldehyde (*m/z* 30), propene (*m/z* 42), ethenol and acetaldehyde (*m/z* 44), and acetone and propanal (*m/z* 58). Additionally, the relative concentrations of these products are plotted in Fig. 3f as a function of temperature. In the following section, we will elucidate their formation mechanisms in the thermal decomposition of *n*-pentyl nitrate with the aid of *ab initio* calculations.

3.2. Thermal decomposition pathways of n-pentyl nitrate

Figure 4 shows the primary decomposition pathways of *n*-pentyl nitrate, based on the CBS-QB3 calculations. Since the conformational isomers of *n*-pentyl nitrate are almost isoenergetic (ΔE<0.4 kcal·mol^{-1} at the CBS-QB3 level) and the isomerization barriers for these conformers are low (~2 kcal·mol^{-1}), we only show the most stable conformer of *n*-pentyl nitrate here. The structures and relative energies of four lowest isomers are summarized in Table S2 and Table S3. The relative energies for these primary decomposition pathways calculated at the CBS-QB3 level

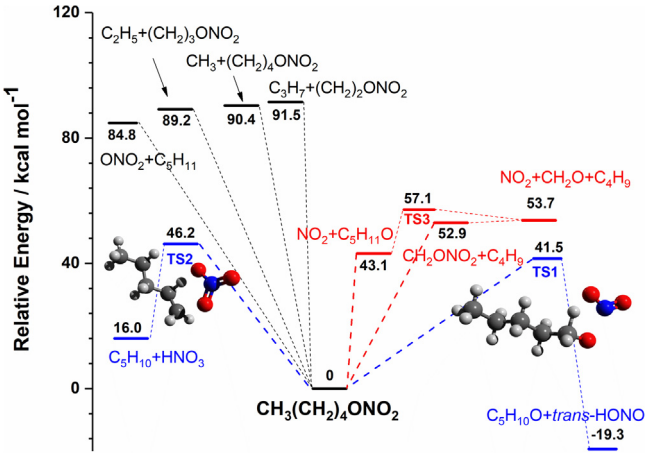

Fig. 4. Calculated primary decomposition pathways of *n*-pentyl nitrate at the CBS-QB3 level. The energies are relative to the neutral *n*-pentyl nitrate molecule. The red lines show the most feasible direct bond-fission pathways, while the blue lines indicate the H-migration/dissociation channels.

are listed in Table 1. Among all direct bond-fissions (**R1-R6**) of *n*-pentyl nitrate, the most feasible pathway **R1** is endothermic by 43.1 kcal·mol^{-1} to produce NO_2 and pentyloxy radical ($C_5H_{11}O$•), which is in good agreement with the previous calculations of nitrate esters [14]. The primary product, NO_2, was indeed observed in the experiment (Fig. 1). In contrast, the bond breaking of the C–O bond (**R2**) can produce •ONO_2 and pentyl radicals by absorbing 88.2 kcal·mol^{-1}. This energy is comparable to that of the C–C bond-fission process, e.g., 90.4 kcal·mol^{-1} for methyl loss (**R6**), 89.2 kcal·mol^{-1} for ethyl loss (**R5**), and 91.5 kcal·mol^{-1} for propyl loss (**R4**). Apparently, such strongly endothermic channels can be neglected in comparison with **R1**. Interestingly, the butyl–loss pathway (**R3**) can produce CH_2ONO_2• (*m/z* 76) and C_4H_9• (*m/z* 57) radicals by overcoming a relatively low barrier of 52.9 kcal·mol^{-1}. Because this energy is not much higher than that of **R1, R3** is also likely to occur in our case. Actually, the corresponding primary product, the C_4H_9• radical, was detected in the experiment, while CH_2ONO_2• was unobserved.

In addition to these direct bond-breaking pathways, isomerization-decomposition reactions have also been explored for the thermal decomposition of *n*-pentyl nitrate. The hydrogen-atom migration from the α-methylene group to the end oxygen atom, followed by N–O bond fission, is found to have the lowest barrier height of 41.5 kcal·mol^{-1} (TS1) to produce nitrous acid (*trans*-HONO, *m/z* 47) and pentanal ($CH_3(CH_2)_3CHO$, *m/z* 86) (**R7**). The overall process is exothermic by 19.3 kcal·mol^{-1}. Another similar H-migration pathway can occur from the β-methylene to the end oxygen atom, followed by C–O bond fission, as noted as **R8** in Table 1. Nitric acid (HNO_3 *m/z* 63) and 1-pentene ($CH_3(CH_2)_2CH{=}CH_2$, *m/z* 70) are the corresponding products. The overall pathway is slightly endothermic by 16.0 kcal·mol^{-1}, and the barrier height (TS2) is calculated to be 46.2 kcal·mol^{-1}. Notably, the ionization potential of HNO_3 is 11.95 eV [32], and the corresponding ion (HNO_3^+) is unstable; thus, NO_2^+ will be formed upon ionization of HNO_3 [33]. As a result, no HNO_3 can be detected in the mass spectra. Despite this, the experimental observation of the other products, *trans*-HONO, pentanal and 1-pentene, confirms the plausibility of the above mechanisms. Additionally, the keto-enol isomerization of pentanal may explain the formation of 4-penten-1-ol indicated in the PIE curve of *m/z* 86 (Fig. 2e).

The subsequent decomposition of the above primary products can generate more species. Following the **R1** pathway, pentyloxy radicals ($C_5H_{11}O$•) can dissociate to formaldehyde

and C_4H_9• radicals via the β-C-C bond fission with a barrier (TS3) of 14.0 kcal·mol^{-1}. The overall process of *n*-pentyl nitrate → NO_2+CH_2O+C_4H_9• needs to overcome a potential of 57.1 kcal·mol^{-1}, as shown in Fig. 4. Interestingly, this activation energy is slightly higher than that of **R3** (52.9 kcal·mol^{-1}), thus stressing that both CH_2ONO_2• and C_4H_9• radicals from the **R3** channel need to be considered in the overall reaction. Considering the decomposition of CH_2ONO_2• radicals, the final products triggered by **R3** are identical to those of **R1** as NO_2+CH_2O+C_4H_9•, but the overall activation energy is slightly lower at 53.7 kcal·mol^{-1} relative to *n*-pentyl nitrate. In summary, there are two formation pathways for formaldehyde (CH_2O, *m/z* 30), NO_2 (*m/z* 46) and C_4H_9• radical (*m/z* 57) along **R1** and **R3**. In view of thermal energetics, the contributions of the two simple bond-fission pathways are comparable. In addition, ethylene (*m/z* 28) and 1-butene (*m/z* 56) can be easily formed from the β-C-C and β-C-H bond breaking of the C_4H_9• radical [34], both of which are observed in the mass spectra (Fig. 2).

There is another important decomposition pathway for the primary products, the $C_5H_{11}O$• radical. As proposed by Davis and Francisco [35], a H-migration/β-C-C bond-fission path with a transition state of a six-membered ring structure can be competitive with the direct β-C-C bond breaking of $C_5H_{11}O$• mentioned above. Propene and •CH_2CH_2OH (C_2H_5O, *m/z* 45) radicals are the corresponding products of this two-step process, and the overall barrier height (TS4 in Fig. S2) is calculated to be 63.9 kcal·mol^{-1}. The internal energy-rich •CH_2CH_2OH radical can readily isomerize to CH_3CH_2O•, and this process is exothermic at 4.2 kcal·mol^{-1} [36]. Then, acetaldehyde can be further formed from H-loss process of CH_3CH_2O•. In addition, another primary product, pentanal ($C_5H_{10}O$, *m/z* 86), produced in **R7** can also decompose to acetaldehyde and propene via a barrier of the five-membered ring structure (TS5 in Fig. S2). It is worth noting that the overall activation energy for this pathway is only 51.6 kcal·mol^{-1} relative to *n*-pentyl nitrate. This value is the lowest among all discussed pathways, thus strongly implying its considerable role in the pyrolysis of *n*-pentyl nitrate. According to the above processes, acetaldehyde and propene can be reasonably formed as we observed in experiments.

Additionally, the C–C bond ruptures of pentanal can further produce more intermediates, such as HCO• (*m/z* 29) and C_4H_9• radicals, C_2H_3O• (*m/z* 43) and C_3H_7• (*m/z* 43) radicals, C_3H_5O• (*m/z* 57) and C_2H_5• (*m/z* 29) radicals, and C_4H_7O• (*m/z* 71) and CH_3• (*m/z* 15) radicals. Notably, these radical products have the same *m/z* as the dissociative photoionization products of *n*-pentyl nitrate, e.g., C_2H_5• (*m/z* 29), C_3H_7• (*m/z* 43), C_4H_9• (*m/z* 57), and C_5H_{11}• (*m/z* 71) radicals; thus, it is difficult to distinguish their sources in this experiment. Fortunately, these products are minor in the pyrolysis of *n*-pentyl nitrate; thus, we do not need to pay more attention to these processes.

In addition, propanal and acetone (both at *m/z* 58) were also observed with a relatively lower peak intensity in Fig. 1. Since these two isomers are interconvertible, we only tried to find the most feasible way to form one of them here. As shown in Fig. S2, propanal can be produced from $C_5H_{10}O$ by overcoming a high barrier of 111.2 kcal·mol^{-1}, which is associated with the release of ethylene. Apparently, such a high barrier hinders the corresponding process. In other words, propanal observed in the experiment is unlikely to be directly formed from the thermal decomposition of *n*-pentyl nitrate. In this sense, we cannot provide a reliable pathway for the formation of propanal and acetone. However, we note, acetone can be formed in the pyrolysis of acetaldehyde at high temperature due to the secondary reaction (2) [37,38],

$$CH_3CHO \rightarrow CH_3\bullet + HCO\bullet \quad (1)$$

$$CH_3\bullet + CH_3CHO \rightarrow CH_3C(O)CH_3 + H \quad (2)$$

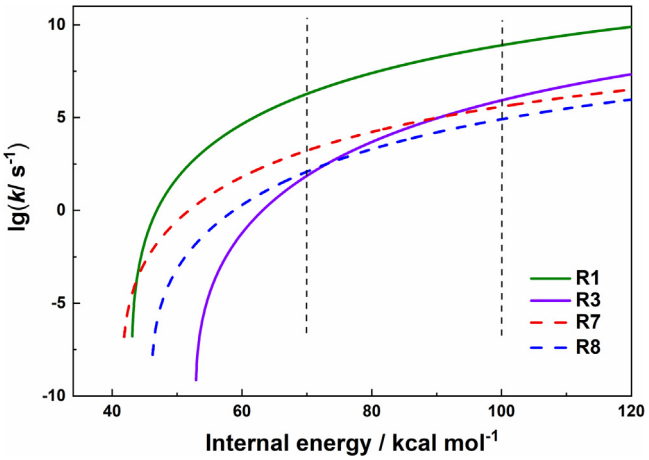

Fig 5. Unimolecular dissociation rate constants for **R1, R3, R7** and **R8** as a function of the internal energy of *n*-pentyl nitrate. Solid lines refer to direct bond fission processes, while dashed lines indicate H-migration/decomposition pathways.

This might imply that some secondary reactions are still involved in our experiments despite the relatively low pressure in the microreactor.

Actually, the β-C-C bond breaking of RO• radicals has been confirmed to dominate its subsequent decomposition, and alkyl groups, aldehydes, and ketones are commonly produced [7–10]. This is generally consistent with our mechanism and provides extra evidence for direct RO–NO_2 bond fission as one of the trigger forces in the pyrolysis of *n*-pentyl nitrate. In addition, NO_2 molecules can be produced either along the bond-fission channels (**R1** and **R3**) or the H-migration/dissociative photoionization path (**R8**); thus, it is rightfully dominant among all products in the thermal decomposition of *n*-pentyl nitrate.

3.3. Branching ratio of major pathways in the pyrolysis of n-p*entyl* nitrate

Although the formation mechanisms of most products observed in mass spectra are proposed above, direct bond-fission or H-migration for thermal decomposition of *n*-pentyl nitrate have very close barrier heights. Thus, it is difficult to determine which of these two pathways is the most significant trigger force, relying only on thermal energetics. Therefore, the corresponding microcanonical reaction rates are necessary to estimate branching ratios and to make a reliable judgment. Based on the calculated decomposition pathways in Fig. 4, RRKM theory [17,39] was employed to estimate the branching ratios over the various products in the primary decomposition of *n*-pentyl nitrate. For the direct bond-fission processes such as **R1-R6**, no saddle points were found; thus, we used the vibrational frequencies at a constrained 3.5 Å bond length along the reaction coordinate as the approximate values of each loose transition state. For **R7** and **R8**, the vibrational frequencies of the located transition state were directly used. As mentioned above, only **R1, R3, R7** and **R8** are taken into account, while the others are neglected due to their excessively high activation energies.

Figure 5 plots the calculated microcanonical rate constants for these four primary pathways. At an internal energy of 70 kcal·mol^{-1} of *n*-pentyl nitrate, the main branching ratios were determined to be 46.7% for **R1**, 13.9% for **R3**, 23.9% for **R7**, and 15.5% for **R8**. Direct RO–NO_2 bond fission is dominant. Thus, the concentration of NO_2 is naturally higher than that of *trans*-HONO, which agrees with the experimental result (in Table 1). When the inter-

Table 3
The computed relative energies for the four dominant primary decomposition pathways of C2-C5 nitrates at the CBS-QB3 level relative to the respective neutral nitrates.

	pathways	relative energy /kcal·mol^{-1}				description
		C2	C3	C4	C5	
R1	RO + NO_2	42.9	42.9	42.9	43.1	N–O bond fission
R3	R′ + CH_2ONO_2	53.2	52.2	52.9	52.9	C–C bond fission
R7	RHO + *trans*-HONO	−19.9	−19.3	−19.9	−19.3	pentanal formation
R8	R″=CH_2 + $HONO_2$	18.4	15.7	16.0	16.0	1-pentene formation

nal energy is increased to 100 kcal·mol^{-1}, the **R3** and **R8** ratios are improved to 23.4% and 19.4%, respectively, while those of **R1** and **R7** drop to 35.1% and 22.1%, respectively. As a result, the concentrations of NO_2 (from **R1**) and *trans*-HONO (from **R7**) are reduced with temperature, but that of formaldehyde (from **R3**) is improved. These results are generally consistent with the experimental data in Table 2.

3.4. General primary decomposition pathways in the pyrolysis of n-alkyl nitrates

Based on the above discussions, we further modeled the potential energy surface for the primary thermal decomposition of C2-C4 nitrates (i.e., ethyl nitrate, n-propyl nitrate, and n–butyl nitrate), and the energetics of the major initial processes were calculated. As shown in Table 3, the activation energies of these pathways, **R1, R3, R7** and **R8,** for C2-C5 nitrates are very close. Therefore, similar to the case of *n*-pentyl nitrate, both direct bond fission (**R1** and **R3**) and hydrogen migration (**R7** and **R8**) are potential driving forces for the thermal decomposition of n-alkyl nitrates with a moderate carbon chain length.

4. Conclusions

Pyrolysis of *n*-pentyl nitrate was conducted with the products and intermediates detected using VUV synchrotron photoionization mass spectrometry. According to the measured PIE curves and IE_a values, major intermediates and products were identified, such as ethylene, formaldehyde, propene, ethenol, acetaldehyde, 1-pentene, pentanal, 4-penten-1-ol, NO_2, and *trans*-HONO.

To obtain new insights into the thermal decomposition mechanism of *n*-pentyl nitrate, quantum chemical calculations at the CBS-QB3 level of theory were performed. As the most feasible pathway for the primary decomposition of *n*-pentyl nitrate, $C_5H_{11}O$• radicals and NO_2 are expected to be formed in the RO–NO_2 bond fission process, and further dissociation leads to butyl radicals and formaldehyde. Similarly, butyl radicals and CH_2ONO_2 can be produced from the direct β-C-C bond fission of *n*-pentyl nitrate, and CH_2ONO_2 can easily decompose to formaldehyde and NO_2. These two pathways have close activation energies and play a dominant role together in *n*-pentyl nitrate pyrolysis.

In addition, two hydrogen-atom migration channels followed by decomposition are also theoretically revealed in the primary thermal decomposition of *n*-pentyl nitrate. Although they have lower barrier heights than those of direct bond fission pathways, our RRKM calculations verify their minor roles in the overall decomposition process due to their relatively slow rates. However, their contributions still cannot be ignored, according to the experimental observation of *trans*-HONO, pentanal, and 1-pentene. Additionally, the small molecule products observed in the experiment are formed from further decomposition of intermediates or secondary reactions.

Our experimental and theoretical investigation provides solid evidence to highlight both bond fission and hydrogen migration as potential driving forces in the overall pyrolysis process. This thermal decomposition mechanism of *n*-pentyl nitrate can provides some useful clues for developing combustion models of long chain nitrates in future.

Declaration of Competing Interest

The authors declare that they have no known competing financial interests or personal relationships that could have appeared to influence the work reported in this paper.

Acknowledgments

The work was financially supported by National Natural Science Foundation of China (No. 51976208, 21873089, 21903079) and by the Hefei Science Center, CAS (2020HSC-KPRD001, 2021HSC-UE005).

Supplementary materials

Supplementary material associated with this article can be found, in the online version, at doi:10.1016/j.combustflame.2022.112576.

References

[1] S. Fordham, High Explosives and Propellants, 2nd ed., Pergamon Press, New York (1980), pp. 35–45.
[2] P.W. Cooper, Explosives Engineering: USA, John Wiley&Sons Inc (1996), pp. 33–165.
[3] Z. Svatopluk, Kinetic compensation effect and thermolysis mechanisms of organic polynitroso and polynitro compounds, Therinochiin. Acta 290 (1997) 199–217.
[4] P.Q. Clothier, D. She, A. Moise, H.O. Pritchard, Stimulation of diesel-fuel ignition by benzyl radicals, Combust. Flame 101 (1995) 383–386.
[5] P.Q. Clothier, H.O. Pritchard, M.A. Poirier, Synergy between additives in stimulating diesel-fuel ignition, Combust. Flame 95 (1993) 427–429.
[6] J.B. Levy, F.J. Adrian, The thermal decomposition of nitrate Esters-III. n-Propyl nitrates, J. Am. Chem. Soc. 77 (1955) 2015.
[7] J.F. Griffiths, M. Gilliigan, P. Gray, Pyrolysis of isopropyl nitrate-I. Decomposition at low temperatures and pressures, Combust. Flame 24 (1975) 11–19.
[8] J.F. Griffiths, M.F. Gilligan, P. Gray, Pyrolysis of isopropyl nitrate-II. Decomposition at high temperatures and pressures, Combust. Flame 26 (1976) 385–393.
[9] J.C. Oxley, J.L. Smith, W. Ye, E. Rogers, A.A. Aradi, T. Henly, Fuel combustion additives: a study of their thermal stabilities and decomposition pathways, Energy Fuels 14 (2000) 1252–1264.
[10] H.O. Pritchard, Thermal decomposition of isooctyl nitrate, Combust. Flame 75 (1989) 415–416.
[11] J. Morin, Y. Bedjanian, Kinetic and mechanistic study of the thermal decomposition of ethyl nitrate, Int. J. Chem. Kinet. 49 (2017) 354–362.
[12] J. Morin, Y. Bedjanian, Thermal decomposition of isopropyl nitrate: kinetics and products, J. Phys. Chem. A 120 (2016) 8037–8043.
[13] J. Morin, Y. Bedjanian, Thermal decomposition of n-propyl and n-butyl nitrates: kinetics and products, J. Anal. Appl. Pyrol. 124 (2017) 576–583.
[14] X.L. Zeng, W.H. Chen, J.C. Liu, J.L. Kan, A theoretical study of five nitrates: electronic structure and bond dissociation energies, J. Mol. Struct. (Theochem) 810 (2007) 47–51.
[15] S. Wang, R. Kong, X. Shan, Y. Zhang, L. Sheng, Z. Wang, L. Hao, S. Zhou, Performance of the atomic and molecular physics beamline at the National Synchrotron Radiation Laboratory, J. Synchrotron. Radiat. 13 (2006) 415–420.
[16] B. Sztaray, K. Voronova, K.G. Torma, K.J. Covert, A. Bodi, P. Hemberger, T. Gerber, D.L. Osborn, CRF-PEPICO: double velocity map imaging photoelectron photoion coincidence spectroscopy for reaction kinetics studies, J. Chem. Phys. 147 (2017) 013944.

[17] T. Yu, X. Wu, X. Zhou, A. Bodi, P. Hemberger, Hydrogen migration as a potential driving force in the thermal decomposition of dimethoxymethane: new insights from pyrolysis imaging photoelectron photoion coincidence spectroscopy and computations, Combust. Flame 222 (2020) 123–132.
[18] http://flame.nsrl.ustc.edu.cn/database/. National Synchrotron Radiation Laboratory, Hefei, China. (2017)
[19] J.A. Montgomery, M.J. Frisch, J.W. Ochterski, G.A. Petersson, A complete basis set model chemistry. VI. Use of density functional geometries and frequencies, J. Chem. Phys. 110 (1999) 2822–2827.
[20] H.P. Hratchian, H.B. Schlegel, Using Hessian updating to increase the efficiency of a Hessian based predictor-corrector reaction path following method, J. Chem. Theory. Comput. 1 (2005) 61–69.
[21] S. Grimme, J. Antony, S. Ehrlich, H. Krieg, A consistent and accurate ab initio parametrization of density functional dispersion correction (DFT-D) for the 94 elements H-Pu, J. Chem. Phys. 132 (2010) 154104.
[22] M.J. Frisch, G.W. Trucks, H.B. Schlegel, G.E. Scuseria, M.A. Robb, J.R. Cheeseman, G. Scalmani, V. Barone, G.A. Petersson, H. Nakatsuji, et al., Gaussian 16, Revision A.03, Gaussian, Wallingford, CT, 2016.
[23] K.S. Haber, J.W. Zwanziger, F.X. Campos, R.T. Wiedmann, E.R. Grant, Direct determination of the adiabatic ionization potential of NO_2 by multiresonant optical absorption, Chem. Phys. Lett. 144 (1988) 58–64.
[24] J.W. Au, C.E. Brion, Absolute oscillator strengths for the valence-shell photoabsorption (2-200eV) and the molecular and dissociative photoionization (11-80eV) of nitrogen dioxide, Chem. Phys. 218 (1997) 109–126.
[25] C.A. Taatjes, D.L. Osborn, T.A. Cool, K. Nakajima, Synchrotron photoionization measurements of combustion intermediates: the photoionization efficiency of HONO, Chem. Phys. Lett. 394 (2004) 19–24.
[26] J.L. Holmes, F.P. Lossing, P.C. Burgers, The need for adequate thermochemical data for the interpretation of fragmention mechanisms and ion structure assignments, Int. J. Mass Spectrom. Ion Phys. 47 (1983) 133–136.
[27] R. Hernandez, P. Masclet, G. Mouvier, Spectroscopie de photoelectrons d'aldehydes et de cetones aliphatiques, J. Electron. Spectrosc. Relat. Phenom. 10 (1977) 333–347.
[28] T.A. Cool, J. Wang, K. Nakajima, C.A. Taatjes, A. McLlroy, Photoionization cross sections for reaction intermediates in hydrocarbon combustion, Int. J. Mass Spectrom. 247 (2005) 18–27.
[29] L.G. Dodson, L. Shen, J.D. Savee, N.C. Eddingsaas, O. Welz, C.A. Taatjes, D.L. Osborn, S.P. Sander, M. Okumura, VUV photoionization cross sections of HO_2, H_2O_2, and H_2CO, J. Phys. Chem. A 119 (2015) 1279–1291.
[30] J.C. Traeger, A study of the allyl cation thermochemistry by photoionization mass spectrometry, Int. J. Mass Spectrom. Ion Processes. 58 (1984) 259–271.
[31] T.A. Cool, K. Nakajima, T.A. Mostefaoui, F. Qi, A. Mcllroy, P.R. Westmoreland, M.E. Law, L. Poisson, D.S. Peterka, M. Ahmed, Selective detection of isomers with photoionization mass spectrometry for studies of hydrocarbon flame chemistry, J. Chem. Phys. 119 (2003) 8356–8365 (2003) 8356-8365.
[32] H.W. Jochims, W. Denzer, H. Baumgärtel, O. Lösking, H. Willner, Photochemical decay reactions of N_2O_5, HNO_3, $ClNO_3$ and $BrNO_3$ in the energy range 10-20eV, Ber. Bunsenges. Phys. Chem. 222 (2020) 123–132.
[33] D.R. Lloyd, P.J. Roberts, I.H. Hillier, Electronic structure of nitric acid studied by photoelectron spectroscopy and molecular orbital calculation, J. Chem. Soc. Faraday Trans. 71 (1975) 496–502.
[34] J.C. Schultz, F.A. Houle, J.L. Beauchamp, Photoelectron spectroscopy of 1-propyl, 1-butyl, isobutyl, neopentyl, and 2-butyl radicals: free radical precursors to high-energy carbonium ion isomers, J. Am. Chem. Soc. 106 (1984) 3917–3927.
[35] A.C. Davis, J.S. Francisco, Reactivity trends within alkoxy radical reactions responsible for chain branching, J. Am. Chem. Soc. 133 (2011) 18208–18219.
[36] D.W.H. Rankin, CRC Handbook of Chemistry and Physics, 89th edition, edited by David R. Lide, Crystallogr Rev 15 (2009) 223–224.
[37] L. Batt, Acetone formation in the pyrolysis of acetaldehyde, J. Chem. Phys. 47 (1967) 3674–3675.
[38] M.T.H. Liu, K.J. Laidl, Elementary processes in the acetaldehyde pyrolysis, Can. J. Chem. 46 (1968) 479–490.
[39] B. Sztaray, A. Bodi, T. Baer, Modeling unimolecular reactions in photoelectron photoion coincidence experiments, J. Mass. Spectrom. 45 (2010) 1233–1245.